

Combined approach to the Hubble Space Telescope wave-front distortion analysis

Claude Roddier and François Roddier

Stellar images taken by the Hubble Space Telescope at various focus positions have been analyzed to estimate wave-front distortion. Rather than using a single algorithm, we found that better results were obtained by combining the advantages of various algorithms. For the planetary camera, the most accurate algorithms consistently gave a spherical aberration of $-0.290\text{-}\mu\text{m}$ rms with a maximum deviation of $0.005\text{ }\mu\text{m}$. Evidence was found that the spherical aberration is essentially produced by the primary mirror. The illumination in the telescope pupil plane was reconstructed and evidence was found for a slight camera misalignment.

Key words: Space telescope, wave-front sensing, phase retrieval, aberrations.

1. Introduction

The observation of defocused stellar images has long been known as a sensitive test for mirror figure errors. However, there have been few attempts to extract quantitative information from such images. Recently we proposed a method based on geometrical optics, which is valid only for highly defocused images.¹ The method consists of taking the difference in illumination between two defocused images as a map of the local wave-front Laplacian. The wave front is reconstructed by solving a Poisson equation. The method is comparable in sensitivity to a Hartmann test² and has been successfully used to control the optical quality of telescopes on Mauna Kea.³ Because the method is based on the geometrical optics approximation, it works with broadband, extended light sources such as stellar sources blurred by atmospheric turbulence.

In the framework of the Hubble Aberration Recovery Program (HARP) organized by the Jet Propulsion Laboratory (JPL), we requested that highly defocused images be taken in flight by the Hubble Space Telescope (HST) so that the method could be applied to estimate the exact amount of spherical aberration. Because defocusing the image also defocuses the telescope tracking system, it was not possible to obtain images sufficiently defocused for the method to apply. However, defocused images recorded by

the HST are not blurred by the atmosphere and can be taken through narrow-band filters. In this case the wave-front information is still preserved and can be recovered by using phase-retrieval algorithms. As we shall see, the image blur that is due to telescope jitter then becomes a limitation.

The first practical phase-retrieval algorithm was described by Gerchberg and Saxton.⁴ This algorithm uses a single in-focus image rather than two defocused images. In addition, the pupil transmission function is assumed to be known. One starts with a first guess of the incoming wave-front phase (which can be random) and computes the diffracted amplitude and phase in the image plane by taking the Fourier transform of the input complex wave front. The calculated amplitude is then replaced by the observed amplitude (square root of the image intensity). An inverse Fourier transform gives a new estimate of the incoming wave-front phase and amplitude. The calculated amplitude is again replaced by the known incoming wave-front amplitude (given by the pupil transmission function) and the process is iterated. At each step the difference between the known amplitude and the calculated amplitude gives a measure of the current error. Iteration is stopped when the error is below an acceptable level.

At first the algorithm quickly converges but then tends to stagnate. Furthermore, the solution may not always be unique. Fienup and Wackerman⁵ developed methods to avoid stagnation and applied the technique to reconstruct images from the modulus of their Fourier transform. Misell⁶⁻⁸ found that, by using both an in-focus image and an out-of-focus image, ambiguities can be removed and better conver-

The authors are with the Institute for Astronomy, University of Hawaii, 2680 Woodlawn Drive, Honolulu, Hawaii 96822.

Received 24 June 1992.

0003-6935/93/162992-17\$06.00/0.

© 1993 Optical Society of America.

gence can be achieved. The Misell algorithm is now used to test millimetric radio antennas.^{9,10} As in the Gerchberg–Saxton algorithm, the Misell algorithm starts with a first guess for the complex wave front in the telescope entrance pupil and computes the complex amplitude associated with the in-focus image. The calculated amplitude is replaced by the observed amplitude and the result is Fourier transformed back producing a new estimate of the complex amplitude in the telescope pupil plane. However, no constraint is applied in the pupil plane other than by setting to zero any value outside the pupil. The complex amplitude in the pupil plane is multiplied by a quadratic phase factor, which introduces a defocus, and a new Fourier transform is taken that gives an estimate of the complex amplitude in the defocused image. Again the computed amplitude is replaced by the observed amplitude and the result is Fourier transformed back. The process is then iterated.

During the course of this study similar algorithms were developed to adapt the tool to the specific problem posed by HST data. These algorithms were thoroughly tested on simulated data. They are described below. Their advantages and drawbacks are discussed. The results we obtained on the HST are summarized in the following sections. One must emphasize that similar algorithms were also developed by other teams as part of the JPL HARP effort. The results have been published in the final HARP report. Most of the results were presented at the OSA topical meeting on Space Optics for Astrophysics and Earth and Planetary Remote Sensing, held in Williamsburg. Some results have also been presented at various SPIE Conferences (e.g., vols. 1542 and 1567). Our results were generally found to be in good agreement with those of others.

2. Algorithms

A. Modified Misell Algorithm

From our previous experience in reconstructing wave fronts it was clear that highly defocused images were still necessary to retrieve the wave front with good spatial resolution, because highly defocused images make better use of the detector dynamic range, can be used with larger optical bandwidths, and are less sensitive to telescope jitter. In the Misell algorithm, the complex amplitude in a defocused image is computed by multiplying the complex amplitude in the pupil plane by a quadratic phase factor and taking the Fourier transform of the product. However, when the amount of required defocus is large, the associated phase factor may become undersampled, producing aliasing errors. Another possible approach is to take the Fourier transform of the complex wave front first, multiply the result by a defocus phase factor, and Fourier transform back. This second approach gives better results for highly defocused images but it requires the use of two fast Fourier transforms instead of one. In the case of the HST, the phase of the wave front in the pupil plane is affected by spherical aberration. Adding a defocus term may

partially balance the spherical aberration and produce a least-confused image beyond the paraxial focus. When this happens, the phase can still be properly sampled in the pupil plane and the complex amplitude in the defocused image can be computed with a single Fourier transform. For defocused images taken before the paraxial focus, adding a defocus term increases the phase slopes, which in turn requires smaller sampling intervals. These considerations led us to modify the Misell algorithm.¹¹

The algorithm we used is summarized in Fig. 1. It starts with a first guess of the wave-front aberration ($\pm 0.5 \mu\text{m}$) and of the pupil transmission function and computes the complex amplitude for an image (1) recorded beyond the paraxial focus. This can be done by using a single Fourier transform with a defocus factor that is partially balanced by the telescope spherical aberration. The computed amplitude is replaced by the observed amplitude and the result is Fourier transformed back with a different defocus factor that produces the complex amplitude in image (2) that was taken before paraxial focus rather than in the pupil plane. Again the computed amplitude is replaced by the observed amplitude and the result is used to recompute the complex amplitude for image (1). The process continues to iterate back and forth between image (1) and image (2) without ever returning to the pupil plane. As for the Gerchberg algorithm,¹² faster convergence is observed when image (1) is multiplied by an apodization window. The width of the window is increased at each iteration and then the window is suppressed.

As for any Gerchberg–Saxton type algorithm, convergence slows down and stagnates after several iterations. To avoid stagnation, we used the follow-

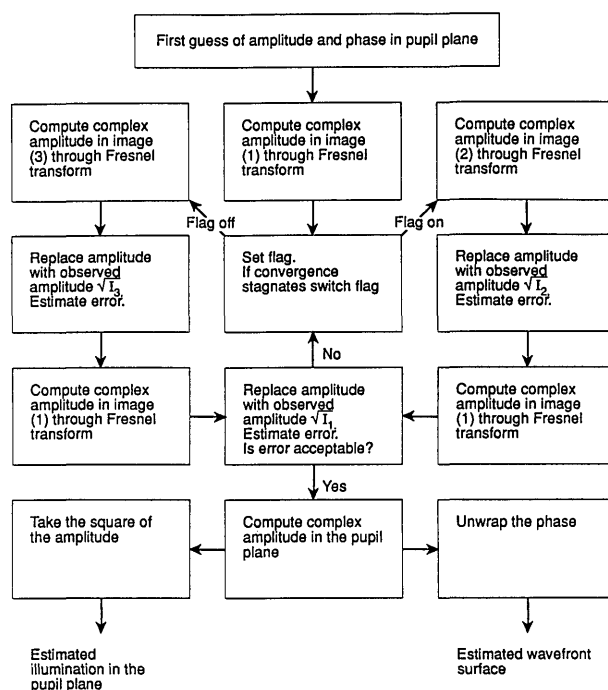


Fig. 1. Flow chart of the modified Misell algorithm.

ing procedure. We omitted image (2) and used our current estimate of the complex amplitude for image (1) to compute the complex amplitude for image (3) by using a single Fourier transform with a different defocus factor. The computed amplitude is replaced by the amplitude observed in image (3) and a new series of iterations is done by iterating back and forth between image (1) and image (3). Convergence becomes rapid again and then slows down. When it stagnates one switches back to iterations between image (1) and image (2) and so forth. This procedure was found to increase convergence but was also found to be sensitive to both decentering and despace errors in the three images. Indeed, as long as only two images are used a decenter error translates into a wave-front tilt; a despace error translates into a wave-front defocus term. Adding a third image requires perfect alignment and correct despace values; otherwise convergence is affected.

B. Original Misell Algorithm

One advantage of the original Misell algorithm, which apparently has never before been used, is the possibility of combining the information from defocused images taken at different wavelengths, because the complex amplitude in the pupil plane is computed at each iteration. One can simply rescale the wave-front phase error in the pupil plane for a different wavelength and similarly compute the diffraction pattern in the image taken at this new wavelength. Also, we wanted to compare the result of our modified Misell algorithm with that of the original algorithm. This motivated us to implement the original Misell algorithm.

It was possible to apply the original Misell algorithm without increasing the sampling frequency by using data taken at longer wavelengths for which sampling is not critical. On the same pairs of images both algorithms gave consistent results. However, the original Misell algorithm was found to be sensitive to despace and decenter errors. Because constraints are also applied in the pupil plane, it is indeed equivalent to a three-image algorithm as described above, whereas our modified Misell algorithm is insensitive to despace and decenter errors when only two images are used. For this reason our modified algorithm was found to be superior to the original algorithm.

Because constraints are applied in three different planes, the pupil plane and two image planes, the original Misell algorithm should be compared to our modified algorithm with constraints applied in three image planes. However, because the illumination in the pupil plane is not known accurately enough, only loose constraints can be applied in the pupil plane (illumination outside the pupil is set at zero), whereas strong constraints can be applied in three image planes. This again is an advantage of our modified algorithm.

C. Single-Image Algorithms

We found that algorithms with constraints applied in three different planes are sensitive to despace and

decenter errors. For this reason we preferred our modified algorithm with constraints applied in two image planes only. However, in the case of planetary camera (PC) images a problem still occurs because the pupil geometry strongly depends on the location of the image in the camera and images are never taken exactly at the same location. This led us to investigate the use of algorithms based on a single image, namely, Gerchberg-Saxton type algorithms with full constraints on the amplitude in a single observed defocused image and looser constraints in the pupil plane. We empirically developed the following procedure.

Initially an estimate is used for the large-scale aberrations (here defocus and spherical) and the telescope pupil is modeled as a uniformly illuminated disk (no central obscuration or spider arms). A Fourier transform is used to compute the complex amplitude in the image. The argument or modulus is replaced by the square root of the observed illumination and an inverse Fourier transform is taken that provides a new estimate of the illumination in the pupil plane. Surprisingly this single loop is generally sufficient for the central obscuration and the spider arms to appear as darker areas. Images taken at the secondary mirror position of $-90\text{ }\mu\text{m}$ gave excellent results. By varying the amount of defocus or decenter, one can improve the appearance of the spider arms until they become straight and fairly sharp. Decenter errors tend to distort the reconstructed spider arms, indicating the direction of the decenter. Despace (i.e., focus) errors tend to blur the reconstructed image and also tend to produce a nonuniform illumination in the reconstructed pupil intensity. Either the edge or the center of the pupil is brighter depending on the sign of the focus error. We empirically found this was an accurate way to control the decenter and despace errors. The result is rather insensitive to the estimated spherical aberration. Best results were obtained by refining the centering of the image first until straight spider arms were observed. Additional constraints were then used by setting to zero the illumination in the observed obscured central area. The focus value is then refined until both sharp spider arms and a fairly uniform illumination are observed in the reconstructed pupil. Further constraints can then be optionally applied by also setting to zero the illumination inside the areas that are obscured by the spider arms and the clamp holes in the primary mirror.

Once the pupil geometry is accurately modeled, this model is used to refine our estimate of the defocus and of the spherical aberration. This is done by comparing the observed and the computed images and by minimizing their difference by using the wave-front fitting procedure described in Subsection 2.D. This fitting procedure was found to be more effective than the use of iterative Fourier transforms to retrieve large-scale aberrations. For the sharpest images it was also used to refine the wave-front tilt estimate. On the other hand, iterative Fourier trans-

forms are more effective in retrieving small-scale wave-front structures.

Once wave-front tilt, defocus, and spherical aberration are carefully estimated, these values are used as a first wave-front guess in a regular Gerchberg-Saxton algorithm, together with the determined pupil geometry. At each iteration the pupil geometry and the observed image illumination are used as amplitude constraints, whereas the wave-front phase is left free to evolve. Experience shows that good convergence is observed after 50 iterations without any significant change in the amount of defocus or spherical aberration. Only smaller scale details appear in the reconstructed wave-front phase. After 50 iterations we found that convergence further improves if the constraint of a uniformly illuminated pupil is removed. Approximately five additional iterations with the constraint removed produced stable structures on the pupil illumination. The structures are similar for all the images we processed and could be real as discussed in Section 3.

D. Wave-Front Fitting Procedure

This procedure is applied after a careful determination of the pupil geometry as described in Subsection 2.C. By looking at the spider arms in the pupil image reconstructed from a single-loop Gerchberg-Saxton iteration, one can determine the center of the image within one pixel. This center coincides with the center of the computed image when the comparison is made. We assume that the main low-order wave-front error terms are defocus (Z_4) and spherical aberration (Z_{11}) and use a two-parameter fit. When this comparison was made, we found it essential to take into account any blur in the observed image. Indeed, computed images look sharper than observed images. This is clearly an effect of telescope jitter. Computer simulations showed that trying to match a computed image with a blurred image gives biased results. An excess of defocus provides a better match. The excess of defocus is balanced by an underestimated spherical aberration. Computer simulations also showed that convergence is quite sensitive to the choice of the norm that was used in the comparison. A detailed account of the image-fitting procedure is given in Appendix A.

E. Discussion of Algorithms

From the above descriptions it is clear that each algorithm has its own advantages and drawbacks. Algorithms that use several observed images as constraints are expected to give the most reliable results. Unfortunately they are sensitive to any decenter or despace error. Although less accurate, algorithms based on a single image were found to be extremely useful and helped us to retrieve missing information such as the exact despace and decenter values and the exact pupil geometry for each of the images we processed. Ideally one should process single images first and determine for each of them the exact despace and decenter value and pupil geometry. Images with the same pupil geometry can then be matched

and combined as constraints in a multiple-image algorithm by using accurate despace and decenter values for optimum wave-front reconstruction. This leads us to a combined approach that profits from each algorithm advantage while the drawbacks are minimized.¹³ This approach consists of the following steps:

- (1) Determination of the pupil geometry by applying the Gerchberg-Saxton algorithm to single images.
- (2) Determination of the main aberration terms by using an error minimization algorithm (wave-front fitting).
- (3) Full wave-front reconstruction with a modified Misell algorithm.

Lack of time prevented us from implementing the full procedure on the same images.

We found that image blur that was due to telescope jitter was the main factor that limited the accuracy of the wave-front estimation. The methods we used to overcome this problem are described in detail in Appendix A. It has been claimed that the accuracy of direct pupil-plane to image-plane propagation algorithms is limited and that multiple-plane propagation algorithms that incorporate all the telescope components must be used to get the required accuracy. We disagree with this statement. Direct propagation algorithms simply reconstruct the wave front that, diffracted from infinity, would produce the recorded image regardless of how the image was actually produced. Some inaccuracy may come from *a priori* assumptions made on the pupil transmission function that may not apply to the actual pupil image as seen from the focal plane through the telescope, because this image may be distorted. Single-image reconstruction algorithms indeed require *a priori* assumptions such as the existence of straight spider arms and a fairly uniform pupil illumination. Moreover these algorithms are necessarily blind to aberrations that are produced in a plane conjugate to the image because these aberrations cannot affect their illumination. However, as soon as more than one image is used, all the wave-front aberrations are taken into account and no *a priori* assumption is needed on the pupil configuration. Our approach was to minimize such assumptions. When they were made, the assumptions were used to boost algorithm convergence and were later removed. We suspect that multiple-plane propagation algorithms may seem to produce more consistent results simply because they tend to produce images with more blur, which reduces the error that is due to telescope jitter. Neither direct nor multiple-plane propagation algorithms give information on the origin of the observed wave-front aberration unless several images are used at different field positions (see Subsection 4.G).

3. Image Analysis

The data we used are displayed in Table 1. They are divided into four main sets. The results obtained

Table 1. Hubble Space Telescope Data Used in This Study

Date	JPL No.	Camera	Filter	Focus	Coordinates	Defocus ($\mu\text{m rms}$)	Spherical ($\mu\text{m rms}$)
First set of data							
8/31	w24318	PC6	F487N	-5	448, 381	-0.7	
9/4	w24706	PC6	F487N	+250	451, 382	+0.87	
9/4	w24730	PC6	F487N	-90	450, 378	-1.18	
9/5	w24818	PC6	F487N	-260	454, 378	-2.25	-0.294 ^a
9/4	w24710	PC6	F889N	+250	450, 382	+0.89	
9/4	w24734	PC6	F889N	-90	451, 379	-1.15	-0.288 ^a
Second set of data							
10/25	w29826	PC6	F889N	-267	532, 425	-2.32	
10/25	w29830	PC6	F889N	-267	532, 425	-2.32	
10/25	w29906	PC6	F889N	-260	530, 426	-2.27	
10/25	w29910	PC6	F889N	-260	531, 425	-2.27	
10/25	w29918	PC6	F889N	+170	537, 419	+0.2	-0.278
10/25	w29826	PC6	F889N	-267	532, 425	-2.32	
10/25	w29830	PC6	F889N	-267	532, 425	-2.32	
10/25	w29906	PC6	F889N	-260	530, 426	-2.27	
10/25	w29910	PC6	F889N	-260	531, 425	-2.27	
10/25	w29930	PC6	F889N	+210	538, 421	+0.42	-0.270
11/30	w33434	PC6	F631N	-90	713, 674	-1.12	
12/3	w33714	PC6	F889N	+333	671, 677	+1.25	-0.298
Third set of data							
12/3	w33702	PC6	F889N	+333	196, 228	+1.28	-0.305
12/3	w33706	PC6	F889N	+333	680, 158	+1.25	-0.294
12/3	w33710	PC6	F889N	+333	143, 674	+1.25	-0.300
12/3	w33726	PC6	F889N	+333	487, 495	+1.26	-0.302
10/26	w29938	PC6	F613N	+250	538, 422	+0.83	-0.292
11/30	w33402	PC6	F613N	-90	190, 221	-1.184	-0.292 ^a
11/30	w33406	PC6	F613N	-90	453, 336	-1.216	-0.289 ^a
11/30	w33410	PC6	F631N	-90	717, 337	-1.252	-0.295 ^a
11/30	w33414	PC6	F631N	-90	184, 595	-1.205	-0.292 ^a
11/30	w33422	PC6	F631N	-90	716, 412	-1.230	-0.288 ^a
11/30	w33426	PC6	F631N	-90	183, 670	-1.200	-0.288 ^a
11/30	w33430	PC6	F631N	-90	447, 672	-1.220	-0.286 ^a
11/30	w33434	PC6	F631N	-90	713, 674	-1.253	-0.291 ^a
Fourth set of data							
		FOC	F486N	-90		-1.1	-0.245
		FOC	F486N	+250		0.8	-0.248

^aThe most reliable values of spherical aberration.

from each of these four sets are described in separate sections. Each set is divided into subsets of images that were processed together. The focus column gives the secondary mirror despace in micrometers. The star coordinates are given in pixel numbers on the detector. The last two columns list the defocus term that is estimated for each image and the spherical aberration term estimated for each subset. The most reliable values of the spherical aberration are marked by an asterisk.

A. Analysis of the First Set of Data

We started our analysis with the images of the first set of data taken at 0.487 μm . The modified Misell algorithm described in Fig. 1 was used. This algorithm uses thru images labeled (1), (2), and (3). Image (1) is used at each iteration. To limit the amount of computing time we used 256×256 arrays and found that the aberrated image at the paraxial

focus was already too large to be accurately reproduced without aliasing errors by taking the Fourier transform of the estimated complex amplitude in the pupil plane. We therefore decided to take image (1) near the circle of least confusion (focus position 250). Images (2) and (3) were taken as far as possible from image (1), at focus positions -90 and -260. These positions are shown in Fig. 2. To minimize interpolation errors, we set the size of the telescope pupil at 65.71 pixels, which gave us computed images with the following sampling: 7.5 μm pixels for image (1), which is half of the data pixel size; 15 μm pixels for image (2), which is the camera pixel size; 22.2 μm pixels for image (3), the only image that required interpolation.

Several runs were made by using slightly different initial guesses and by varying the order of iterations. In each case an estimate of the complex amplitude in the telescope pupil plane was obtained. All the

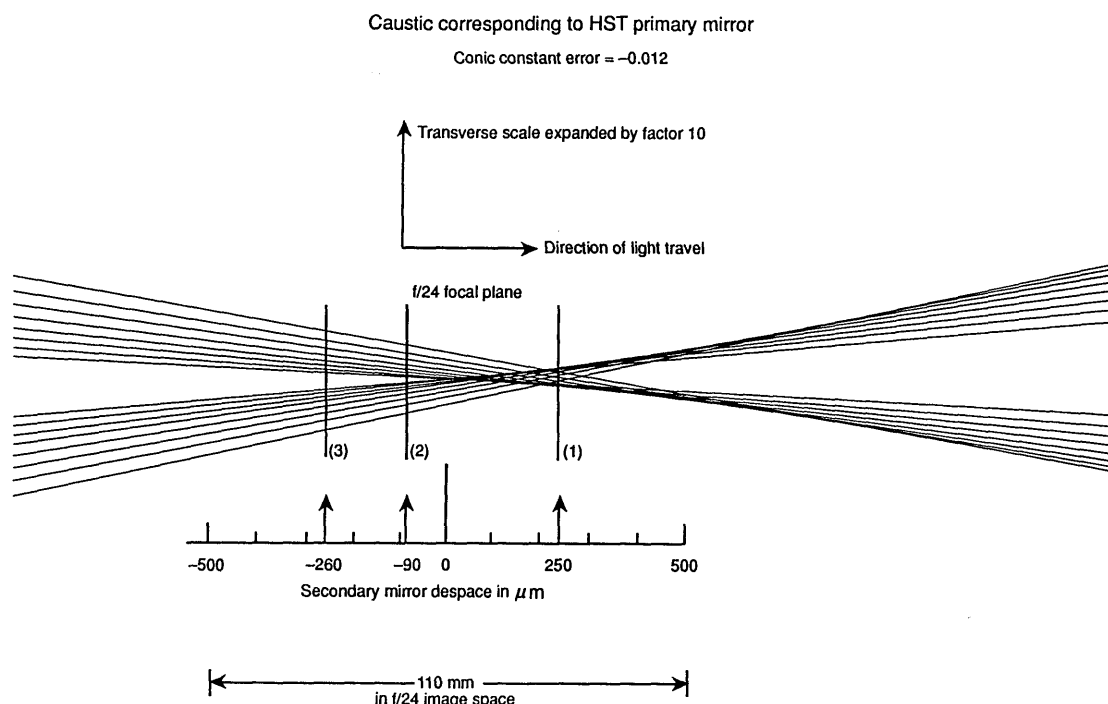


Fig. 2. Ray tracing showing the effect of spherical aberration at the focal plane of the Hubble Space Telescope (courtesy A. Vaughan). The modified Misell algorithm was applied to images labeled (1), (2), (3) taken at $0.487 \mu\text{m}$ at secondary mirror positions of $+250$, -90 , and -260 .

results were quite similar. Here we give results obtained by averaging all the complex amplitude estimates to produce our final wave-front estimate. From this estimate we computed the illumination in each observed image and compared the result of the computation with the actually observed illumination. The agreement was found to be excellent (see also Subsection 4.F).

Note that, unlike the original Misell algorithm, our modified algorithm does not apply any constraint in the pupil plane. It was still able to reproduce satisfactorily the illumination in the telescope pupil. The reconstructed pupil image clearly showed the central obscuration produced by the PC secondary mirror together with the three thick supporting arms. However, to our surprise they were not centered on the pupil but shifted sideways. Since the images were taken close to the optical axis, the shift showed evidence for a misalignment of the PC. Other evidence for this misalignment was independently found by Burrows¹⁴ from images taken in the wide-field configuration of the camera. A detailed analysis of this misalignment is given in Subsection 4.E.

The illumination on the pupil was found to be nonuniform, showing dark rings. It is not clear whether these rings are real or artifacts. Computation errors tend to produce dark circular zones in the pupil illumination. However, rings appear at nearly the same location in the reconstructed wave-front map and correspond to grooves left by the polishing tool. Because the camera entrance pupil is not conjugate to the telescope pupil and because of the additional telescope spherical aberration these grooves

may indeed diffract light outside the camera entrance pupil, thus producing the observed dark rings in the reconstructed pupil image.

The reconstructed wave front showed almost pure spherical aberration. A least-squares fit of the reconstructed wave front was made with Zernike aberration terms. For best results we used Zernike annular polynomials¹⁵ that are orthogonal over a uniform disk with a 0.33 central obscuration diameter ratio. The fit was made over the illuminated pupil area with the exception of a small region, a few pixels wide, near the pupil edges at which the uncertainty of the reconstructed wave front is quite large. The amplitude of the spherical aberration term was estimated to be $-0.294\text{-}\mu\text{m}$ rms with a dispersion of ± 0.005 . Other terms such as astigmatism, coma, and trefoil were found to be below 4×10^{-3} , that is, within the uncertainty of the estimate. However, smaller scale wave-front errors with an amplitude larger than the uncertainty appeared on the reconstructed wave front. These ringlike structures were found on all the reconstructed wave fronts independent of the algorithm used and are believed to be structures left by the polishing tool on the primary and secondary mirrors. They are described in Subsection 4.D.

The same algorithm was then applied to a new set of two images taken at a longer wavelength (next subset in Table 1). These images were taken on 4 September at $0.889 \mu\text{m}$ at focus positions $+250$ and -90 . Using images taken at a longer wavelength has the effect of relaxing constraints on the sampling of the quadratic phase factors, allowing us to keep working with 256×256 arrays with a minimum of

aliasing errors. On this set the spherical aberration term was estimated to be $-0.228\text{-}\mu\text{m}$ rms with a dispersion of ± 0.005 . The other Zernike terms were again found to be all below 0.004, that is, within the uncertainty of the measurement. From the reconstructed pupil image we have estimated that the camera spider arms should coincide with the telescope spider arms when the star image coordinates are in pixels 210 ± 50 and 300 ± 50 . A more detailed analysis of the camera misalignment is given by the third set of data used.

B. Analysis of the Second Set of Data

The original Misell algorithm was implemented and applied to this set of data rather than our modified version (see Subsection 2B). It was first applied to the same two images as above (the last two images of the first set) with almost identical results. However, the convergence was found to be slower because of the sensitivity of the algorithm to decenter and despace errors. Since at each iteration this algorithm computes the complex wave front in the pupil plane, we tried to unwrap its phase and each time estimate the wave-front tilt and defocus. The convergence was improved but the algorithm was considerably slowed down. Nevertheless it opened the possibility of using a large set of images in order to maximize the number of constraints.

This was done on the first two subsets of images shown in Table 1, which are identical except for the last image. Again the convergence was found to be poor and the algorithm slow. The final estimate tended to depend on the initial guess used as an input to the algorithm. A low value was found for the spherical aberration term (less than $0.28\text{ }\mu\text{m}$). It is considered to be unreliable. There are several possible explanations. One is that the estimations of the wave-front tilt and defocus made at each iteration are not sufficiently accurate. The other is that the pupil geometry may differ slightly from one image to the other although the images were taken with the star nearly at the same position in the field of view.

Our last attempt to apply the original Misell algorithm was on a pair of images taken at two different wavelengths (0.631 and $0.899\text{ }\mu\text{m}$) with the star image almost at the same location (next subset in Table 1). Again the result tended to depend on the initial guess. In this case a high value was found for the spherical aberration ($0.298\text{ }\mu\text{m}$). It is not considered to be reliable either. It is likely that the pupil geometry for the two images was sufficiently different to prevent good convergence.

C. Analysis of the Third Set of Data

The third set of data was analyzed by using the single-image algorithms described in Subsection 2.C. A single iteration was used to reconstruct an image of the telescope pupil. As discussed above, the reconstructed pupil image was found to be quite sensitive to despace and decenter errors. It was also found to be sensitive to the image blur that was due to telescope jitter, which varies from one image to

another. Figure 3 shows an example of a good reconstructed pupil image.

The method was first applied to images taken at $0.889\text{ }\mu\text{m}$ at focus position +333, which are the five first images of the third set of data. In this case the central obscuration and the spider arms barely appear. Images taken before the focal plane are larger and less sensitive to image jitter and gave the most reliable results. We concentrated our efforts on a series of eight images taken on 30 November at $0.631\text{ }\mu\text{m}$ (the last eight images in Table 1). The first iteration was used to determine the exact location and size of the obscurations produced by both the telescope and the camera secondary mirrors. The pupil was then modeled with uniform illumination and the estimated central obscuration, but still no spider arms. This model was used as the input for a new iteration giving an improved pupil image with sharper spider arms that can be accurately located. This image was used to recover entirely the pupil geometry to be used. This procedure was found to be both simple and effective and was used to map the relative position of the telescope and camera pupils as a function of the star coordinates in the field of view. Table 2 gives the PC pupil offset in pupil-image sample points (pupil radius is 103.05 sample point) as a function of the star coordinates in camera pixel units. The uncertainty on the pupil offset is estimated to be ± 1 pixel.

Once the pupil geometry was determined, we estimated defocus and spherical aberration as described in Appendix A and we used 50 Gerchberg-Saxton iterations to refine our estimate of the complex amplitude in the pupil plane. In addition, five iterations were made with the constraint of uniform pupil illumination removed as described in Subsection 2.C. Table 1 shows the defocus term and the spherical aberration term that have been estimated for each of the eight reconstructed wave fronts.

The eight reconstructed wave fronts were then averaged together and a least-squares fit of the Zernike terms was made on the average wave front as described above. Apart from defocus and spherical aberration, the amplitude of all the terms in between were found to be below $10^{-3}\text{-}\mu\text{m}$ rms. Figure 4 is a map of the reconstructed wave front after removal of

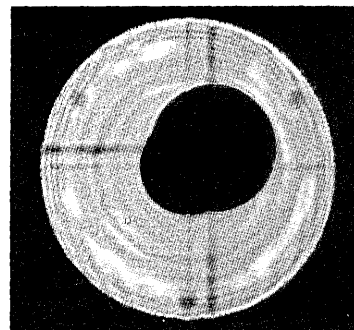


Fig. 3. Example of pupil image reconstructed from a single Gerchberg-Saxton iteration.

Table 2. Camera Pupil Offset as a Function of Star Coordinates

Image No.	x Coordinates	x Offset	y Coordinates	y Offset
w33042	190	-1.5	221	-2.5
w33406	453	7	336	0.5
w33410	717	17.5	337	0.5
w33414	184	-2.5	595	10.5
w33422	716	17.1	412	3
w33426	183	-2.2	670	12.8
w33430	447	7.5	672	12.8
w33434	713	17.1	674	12.6

tilt, defocus, and spherical aberration. These results are consistent with those obtained with the first set of data and are considered to be our most reliable wave-front estimate.

D. Analysis of the Fourth Set of Data

The same single-image algorithm was used to analyze a few stellar images from the faint object camera. Table 1 shows the defocus and spherical aberration terms we have estimated. The uncertainty on the wave front is estimated to be ± 0.01 - μm rms. Other low-order terms were found to be larger than that of the PC but still below the uncertainty. As expected, the reconstructed pupil illumination showed a different geometry from that of the PC (see Subsection 4.E). Best results were obtained with the image taken at focus position -90 .

4. Results

A. Defocus

Table 1 lists the Zernike defocus term in micrometers rms as a function of the secondary mirror position. Theoretically a 1-mm motion of the secondary should produce a 6.135 - μm rms defocus error. A linear regression on the most reliable data (marked by an asterisk) gives a slope of 6.139 $\mu\text{m}/\text{mm}$. This agreement shows the remarkable accuracy of the modified Misell algorithm we used and gives us confidence that a similar level of accuracy can be achieved for the spherical aberration term. The linear regression curve shown in Fig. 5 gives the secondary mirror position for the estimated best focus as follows: best focus position: $+107 \pm 5$ μm .

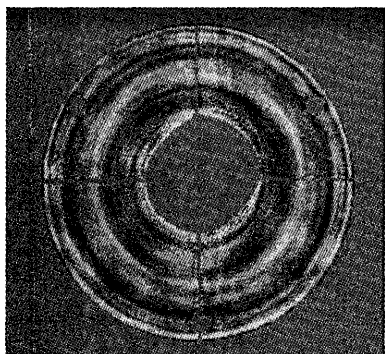


Fig. 4. Reconstructed wave-front surface showing wave-front error residuals after removal of the spherical aberration.

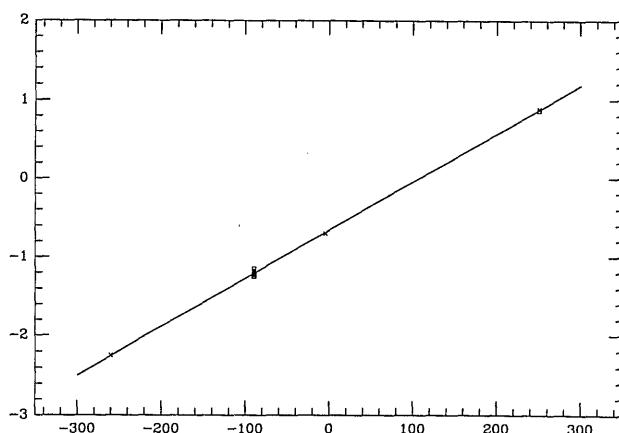


Fig. 5. Linear regression showing the observed defocus terms in micrometers rms as a function of the secondary mirror position in micrometers. Data taken at 0.487 μm (crosses), 0.889 μm (squares), and 0.631 μm (triangles).

By using all the data in Table 1 taken on 4 and 5 September, we estimated the defocus term to be -1.18 ± 0.03 - μm rms at a secondary mirror position of $+90$. By using the data taken on 30 November (last 8 lines in Table 1), we estimated the defocus term to be -1.22 ± 0.025 - μm rms at the same position. Evidence for telescope shrinkage is therefore marginal. If there is any shrinkage it is of the order of 2 $\mu\text{m}/\text{month}$. Given the uncertainty we infer that telescope shrinkage is less than 5 $\mu\text{m}/\text{month}$.

In Subsection 4.F it is shown that a single wave-front model accurately reproduces all the images observed over a 3-month period, providing further evidence that telescope shrinkage is not significant. The FOC data are consistent with the PC results.

B. Spherical Aberration

Taking an average of the most reliable data marked by an asterisk in Table 1 gives for the PC images a wave-front rms spherical aberration term of -0.290 ± 0.0034 - μm rms. The uncertainty given here is the standard deviation. Note that the total deviation is ± 0.005 μm . The FOC data give a significantly smaller value for the spherical aberration. It is estimated to be -0.245 ± 0.01 - μm rms.

C. Other Low-Order Aberration Terms

All the low-order aberration terms between defocus and spherical aberration (astigmatism, coma, trefoil) were found to have an amplitude below the uncertainty level and probably below 10^{-3} - μm rms, showing the remarkable quality of the telescope optics.

D. Mirror Roughness

Figure 4 shows the residual wave-front errors after removal of spherical aberration. Small-scale wave-front residuals are clearly seen with a rms amplitude of approximately 0.02 μm . These small-scale wave-front errors take the form of circular rings and appear to be structures left by the polishing tools both on the primary and the secondary mirrors. A circular zone

can be seen with a mean radius that is equal to 0.65 pupil radius and a width of approximately 0.1 pupil radius. It is $0.04\text{ }\mu\text{m}$ above the surrounding surface. The same zone was independently found on wave fronts that were reconstructed from interferograms of the HST primary mirror taken prior to the launch.¹⁶ It is therefore believed to be real. Smaller rings also appear and are believed to be produced by the telescope secondary.

E. Pupil Geometry

Figure 3 shows an example of reconstructed pupil image. One can see three of the four arms that support the telescope secondary mirror. They are thinner than the camera arms. The fourth arm on the left is hidden behind the camera arm. The distance between the camera arms and the telescope arms is a measure of the camera misalignment. The three black dots at 120° near the pupil outer edge are produced by the three clamps that hold the telescope primary mirror in place. The bottom clamp is directly behind one of the telescope spider arms.

The pupil geometry was reconstructed from such data and discrepancies were found between the reconstructed geometry and the data provided by JPL. The largest discrepancy was evidence for a decenter of the PC pupil with respect to the optical telescope assembly pupil. The amount of decenter is estimated here.

A linear least-squares fit to the data displayed in Table 2 gives the following relationship between the star coordinates (x, y) in camera pixels and the camera pupil offset (X, Y) in pupil image pixels (pupil radius is 103.05 pixels): $x = 27.8X + 245$, $y = 27.8Y + 310$. According to JPL data the slope should be 28.9 instead of 27.8. Figure 6 shows on the same plot the star coordinates effectively used and those computed with the above relations. The uncertainty on the pupil offset is ± 1 pixel in the pupil image that is approximately ± 28 camera pixels. The error boxes in Fig. 6 are 56 camera pixels wide. The

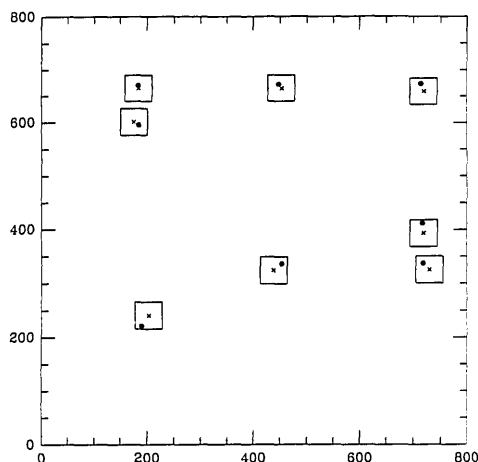


Fig. 6. Star image positions actually measured (dots) and estimated from reconstructed pupil configurations (crosses with error boxes).

offset goes to zero for a star at coordinates $x = 245 \pm 10$, $y = 310 \pm 10$.

The error bar has been divided by the square root of 8 since the results comes from eight independent estimates. The above relationship between the star coordinates and the PC pupil offset was tested on pupil images reconstructed from data taken at secondary mirror positions ranging from +333 to -267. The star coordinates predicted from the observed offset were found to be consistent with the known coordinates every time the spider arms could be accurately located.

Another discrepancy was found with regard to the location of the three clamps that hold the primary mirror. The coordinates of the center of the three clamps were carefully measured on the pupil images that were reconstructed from the same eight images. The rms dispersion for these coordinates is 0.5 pixel or 0.6 cm on the pupil. The rms error for an average of eight measurements is therefore 2 mm. The results of these measurements are shown in Table 3. The coordinates are given in pupil radius units. The coordinates given by JPL were rotated to match the coordinates measured on the lower clamp (see Fig. 3). Clearly the lower clamp is at the expected position, the upper right clamp is 16 mm higher, and the upper left clamp is both 37 mm higher and 6 mm to the right of the expected position. These offsets are well above the uncertainty of the measurement. In addition, we note that the columns of the CCD camera are not quite aligned with the telescope spider arm centered over the lower clamp. The angle is approximately 0.6° .

The pupil image reconstructed from the FOC data shows a different geometry. Compared to the PC the telescope spider arms are clearly rotated 35° clockwise. Since the camera has no pupil-obstructing part its alignment cannot be checked. The location of the clamps approximately confirms the above-described offsets although data may be affected by distortion that is due to the image intensifier.

F. Accuracy of the Reconstructed Wave Front

The above-listed results can be used as a model of the image-forming wave front. This model is comprised of our best reconstructed wave front and the above-determined relationship that gives the pupil offset as a function of the star position in the field of view. From this model it is possible to compute the illumination at any wavelength and focus position for a star anywhere in the field of view. The results of the

Table 3. Location of the Three Clamps Holding the Primary Mirror

Clamp	Coordinate	Measured	JPL Value	Δ	Δ (mm)
1	x	-0.767	-0.772	0.005	6
	y	0.471	0.440	0.031	37
2	x	0.009	0.009	0.000	0
	y	-0.889	-0.890	0.001	1
3	x	0.754	0.755	-0.001	1
	y	0.481	0.468	0.013	16

computation can be used as a point-spread function to deconvolve images that are currently recorded by the telescope. It is therefore important to estimate the accuracy of the model. To check this accuracy we computed a large number of images and compared the result with the actually observed image. The result of this comparison is now shown.

First the comparison was made on the eight images that were used to produce the model, that is, the last eight images of the third set of data in Table 1. As expected, the agreement was found to be excellent. The observed images are clearly blurred by telescope jitter except for one image (w33410) that was noted to be sharp; this image is shown in Fig. 7. The computed image is shown in Fig. 8. Image profiles are shown in Fig. 9 in which the computed image is

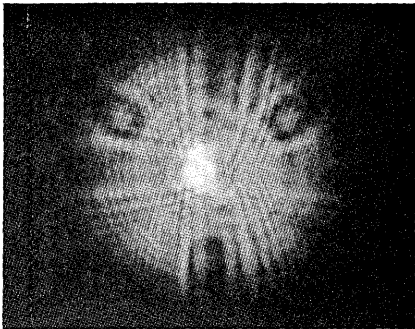


Fig. 7. Image w33410 as observed.

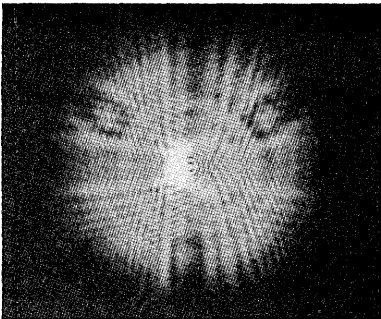


Fig. 8. Image w33410 as computed from the model.

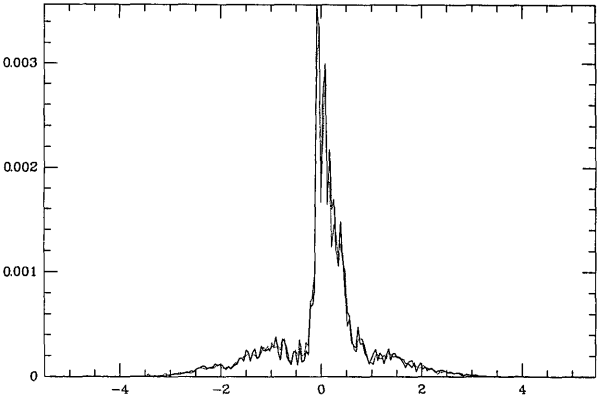


Fig. 9. Comparison between observed (dotted curve) and computed (solid curve) image w33410. The horizontal scale is in arcseconds.

represented by a solid curve, the observed image by a dotted curve.

Next we used the model to compute images over a large range of secondary mirror positions spanning from -267 to $+333$. Figure 10 shows image w29822 and Fig. 11 shows the same image as computed from the model. A cross section of the two images is shown in Fig. 12. Image w29822 was taken a month earlier at position -267 and at a shorter wavelength ($0.487\text{ }\mu\text{m}$). In spite of these differences the agreement is still good. A similar agreement was also found for images w24818 and w24730. These two images were taken two months earlier at positions -260 and -90 and at the same shorter wavelength

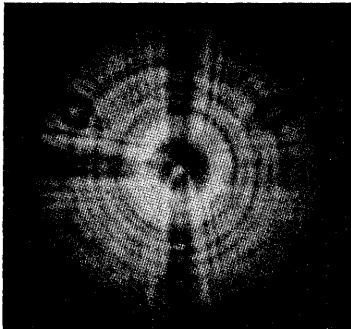


Fig. 10. Image w29822 as observed.

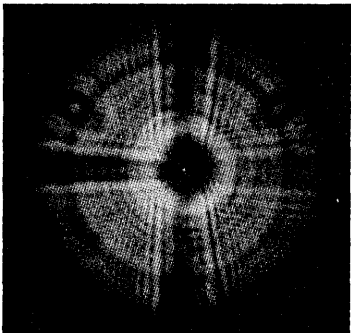


Fig. 11. Image w29822 as computed from the model.

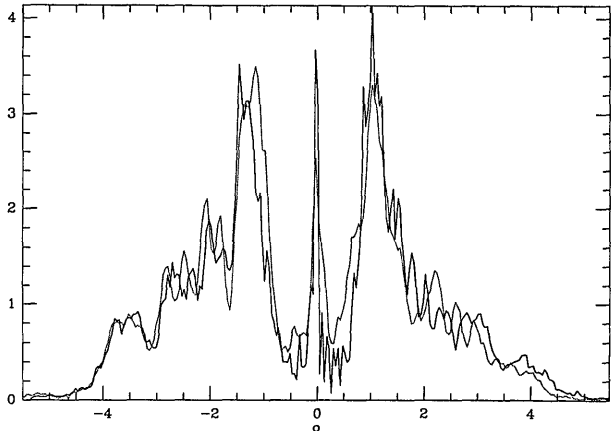


Fig. 12. Comparison between observed (dotted curve) and computed (solid curve) image w29822. The horizontal scale is in arcseconds.

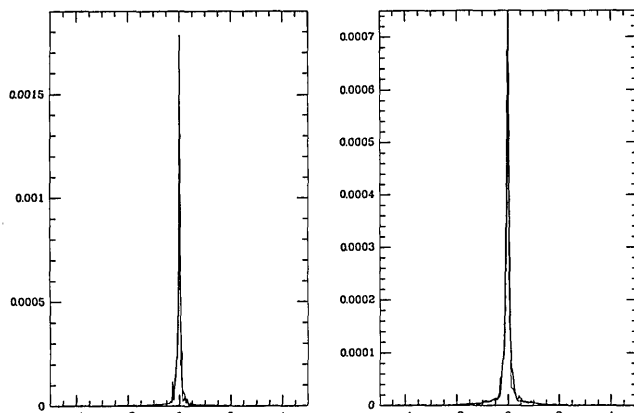


Fig. 13. Comparison between observed (dotted curve) and computed solid curve) image w22718. The computed image is either unblurred (left) or blurred (right). The horizontal scale is in arcseconds.

(0.487 μm). They were used in our modified Misell algorithm (first set in Table 1). The aberration terms and pupil geometry that were obtained with the two different methods were indeed in good agreement.

Figure 13 shows a profile of image w27718 (dotted curve). This image was also taken two months earlier at the same shorter wavelength (0.487 μm) but at position +10, that is, close to best focus. The solid curve shows a profile of the same image computed with our model. The agreement is good. It becomes excellent when the computed image is slightly blurred, simulating the effect of telescope jitter (right). This shows that our model can probably be used to estimate the point-spread function of the PC at any wavelength and anywhere in the field of view. However, the effect of telescope jitter would probably have to be independently estimated by using different stars in the field of view.

The effect of telescope jitter is clearly seen in a comparison with a series of images (w29914, w29922, and w29938) taken at 0.631 μm at positions +170, +210, and +250. In these images the diffraction rings are heavily blurred by telescope jitter and most of the attempts to use these images in a phase-retrieval algorithm were a failure (see Appendix A).

Table 4. Image Pairs Shifted in the x Direction

Image Pairs		Coordinate Difference	
JPL No.		Δx	Δy
w33406	w33410	264	1
w33426	w33430	264	2
w33430	w33434	266	2
w33426	w33434	530	2

They are still fairly well reproduced by the model that produces sharper images. The effect of telescope jitter is particularly dramatic in Fig. 14, which shows image w30014 taken at a shorter wavelength (0.487 μm) at position +333. The computed image is shown in Fig. 15. A blurred version of the computed image is shown in Fig. 16 for better comparison with the observed image.

The above-discussed model does not apply to FOC data because of the different pupil geometry. To reproduce FOC images we used the wave front reconstructed from the image taken at focus position -90 (Table 1). Again good agreement was found between the computed and the observed images at focus positions ranging from -260 to +250.

G. Secondary Mirror Figure

An attempt was made to reconstruct the secondary mirror figure by subtracting wave fronts reconstructed from images taken with the star at different positions in the field of view. For this purpose we used the last eight images in the third set of data in Table 1. These images were taken with different star coordinates that are shown in Fig. 1. We used the wave fronts reconstructed after 50 iterations as described in Subsection 3.C without any further modification. First we subtracted wave fronts reconstructed with star image pairs shifted in the x direction as shown in Table 4. The wave-front difference produced by the last pair in Table 4 was divided by two to account for the two times larger Δx value and the average of the four wave-front differences was taken; this is displayed in Fig. 17. Next we subtracted wave fronts reconstructed with star image pairs shifted in the y direction as shown in Table 5.

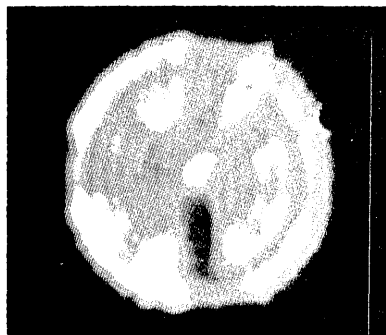


Fig. 14. Image w30014 as observed.

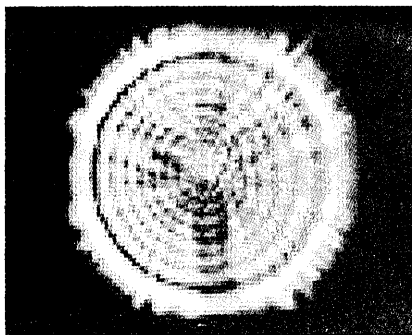


Fig. 15. Image w30014 as directly computed from the model.

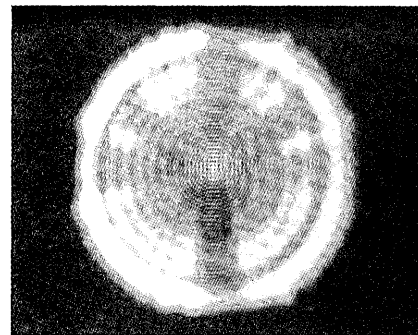


Fig. 16. Image w30014 as computed from the model with additional blur to simulate the effect of telescope jitter.

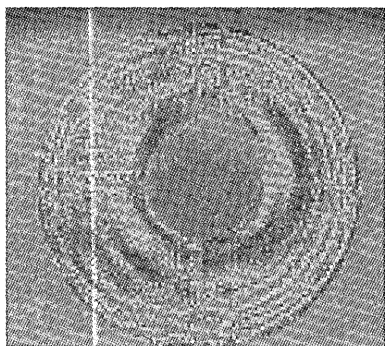


Fig. 17. Secondary mirror x slopes estimated from wave-front differences.

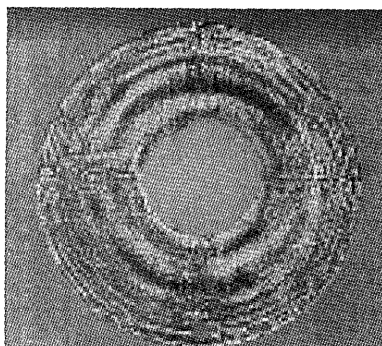


Fig. 18. Secondary mirror y slopes estimated from wave-front differences.

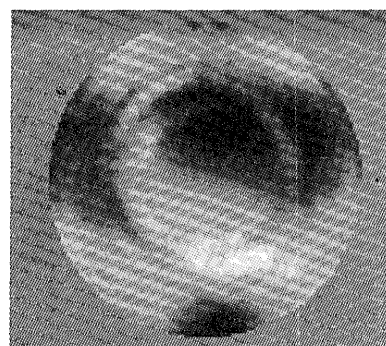


Fig. 19. Secondary mirror figure reconstructed from the slopes shown in Figs. 17 and 18.

Again the average of the three wave-front differences was taken. Its amplitude was scaled down to match a 265-pixel shift similar to the horizontal shift; this is displayed in Fig. 18.

Assuming that the primary mirror is in the pupil plane, its contribution to the wave-front errors should be the same for all the images and should therefore cancel out when the differences are calculated. On the other hand, the contribution of the secondary mirror is slightly shifted in the direction of the image and does not entirely cancel out. With a scale of 0.043 arcsec/pixel for the PC camera, a 265-pixel shift corresponds to an angular deviation of 11.4 arcsec. By assuming that the secondary is at 4.9 m from the primary, this translates into a displacement of a beam of 270 μm on the secondary. Since the 103-pixel aperture diameter corresponds to an illuminated beam size of 267 mm on the secondary, one pixel corresponds to 2.59 mm. Hence the displacement is approximately one tenth of a pixel on the reconstructed wave front.

The question arises whether the structures on the reconstructed wave front reproduce themselves at the same location with that accuracy. It may well be the case. These structures diffract light that interferes with light diffracted by a sharp pupil. Any shift of the structures with respect to the pupil appreciably changes the interference pattern. Since a fixed pupil mask was used as a constraint over 50 Gerchberg-Saxton iterations, the location of the wave-front structures with respect to the pupil mask should be fairly accurate. This is further supported by the aspect of the wave-front differences displayed in Figs. 17 and 18, which closely resembles two knife-edge test patterns taken with the knife edges at 90° from each other. We assume that these wave-front differ-

ences map the wave-front slopes on the secondary mirror, and we reconstructed an estimate of the secondary mirror figure by using a standard algorithm that reconstructs a wave front from its slopes. The result of the integration is shown in Fig. 19. The reconstructed mirror figure shows grooves similar to those left by the polishing tool. Knowing that the 308-mm-diameter mirror is illuminated over only a 267-mm-diameter area, we can see the same grooves nearly at the same position on secondary mirror figures that were obtained before the launch, giving us confidence in the accuracy of our reconstruction. The rms wave-front error in Fig. 19 was estimated to be 0.028 μm . This is to be compared with the secondary mirror figure error estimated to be of the order of 0.01- μm rms from data taken prior to the launch. One reflection on the secondary should therefore produce wave-front errors of the order of 0.02- μm rms in fair agreement with our result. A fit of Zernike terms to the reconstructed wave front gave values that were all below 0.01- μm rms; coma being the largest term. Although there is clearly a lot of uncertainty in the accuracy of this reconstruction, we believe it shows that the contribution of the secondary mirror to the telescope spherical aberration is probably less than 3% and perhaps of the order of the uncertainty on our estimate. In other words, spherical aberration is essentially produced by the telescope primary mirror.

5. Conclusion

The Hubble Space Telescope wave-front distortion has been estimated from stellar images taken in flight at various focus positions. A combination of different phase-retrieval algorithms was used to minimize the effect of despace and decenter errors and uncertainties on the star image position on the CCD camera. Image blur produced by telescope jitter ultimately limited the accuracy of our results.

A total of 30 different planetary camera images were analyzed by using groups of from one to five images. For each group the wave-front surface was reconstructed and fitted with Zernike aberration terms. Different algorithms gave consistent results, and we believe we have determined spherical aberra-

Table 5. Image Pairs Shifted in the y Direction

Image Pairs		Coordinate Difference	
JPL No.		Δx	Δy
w33402	w33414	6	374
w33406	w33430	6	336
w33410	w33434	4	337

tion for the planetary camera with the required accuracy. Our best estimate is $-0.290\text{-}\mu\text{m}$ rms with a maximum deviation of $0.005\text{ }\mu\text{m}$. Other low-order aberration terms were found to be smaller than this deviation and therefore not measurable. However small-scale wave-front errors were detected with a rms amplitude of $0.02\text{ }\mu\text{m}$. They appear as circular rings typically left by a polishing tool and are quite consistent with wave-front errors estimated by combining primary and secondary mirror figures reconstructed from interferograms taken before the launch. Analysis of a few FOC images gave similar results but a lower value for the spherical aberration, $-0.245\text{-}\mu\text{m}$ rms.

An attempt was made to estimate the contribution of the telescope secondary mirror to the aberrations. Evidence was found that the spherical aberration is essentially produced by the primary mirror. We were also able to reconstruct the illumination in the telescope pupil plane. It shows the central obscuration and the spider arms of both the telescope and the camera. These are not superimposed and their relative position varies with the coordinates of the star image on the camera. For PC-6 images the best superposition was found to occur when the star image coordinates were approximately 245 and 310 instead of coordinates 400 and 400 of the field center, showing evidence of camera misalignment.

The methods developed for this study appear to be powerful and can probably be used to model the telescope point-spread function as a function of star coordinates to deconvolve images. The same methods could also be used to check the telescope align-

ment and control its optical performance on a regular basis. For this application we recommend taking a few stellar exposures at $0.631\text{ }\mu\text{m}$ with the secondary mirror set at position $-90\text{ }\mu\text{m}$, conditions that gave us the best results.

We have recently been able to apply the same methods to a ground-based telescope by using short exposures taken in the infrared ($4\text{ }\mu\text{m}$). Seeing effects were reduced to an acceptable level by averaging several reconstructed wave fronts.¹⁷

Appendix A

As discussed in Section 2, low-order aberration terms were estimated from a single image by comparing computed images with the observed image and searching for the minimum difference. A detailed description of the procedure is given here together with a discussion of the errors involved.

1. Effect of Telescope Jitter on the Wave-Front Fitting Procedure

Three different norms were considered as a measure of the image difference. These are labeled N_1 , N_2 , and N_3 :

$$N_1 = \Sigma |I - S|,$$

$$N_2 = [\Sigma (I - S)^2]^{1/2},$$

$$N_3 = \Sigma (\sqrt{I} - \sqrt{S})^2,$$

where I is the observed image and S is the computed image. Figure 20 shows contour plots for N_1 , which

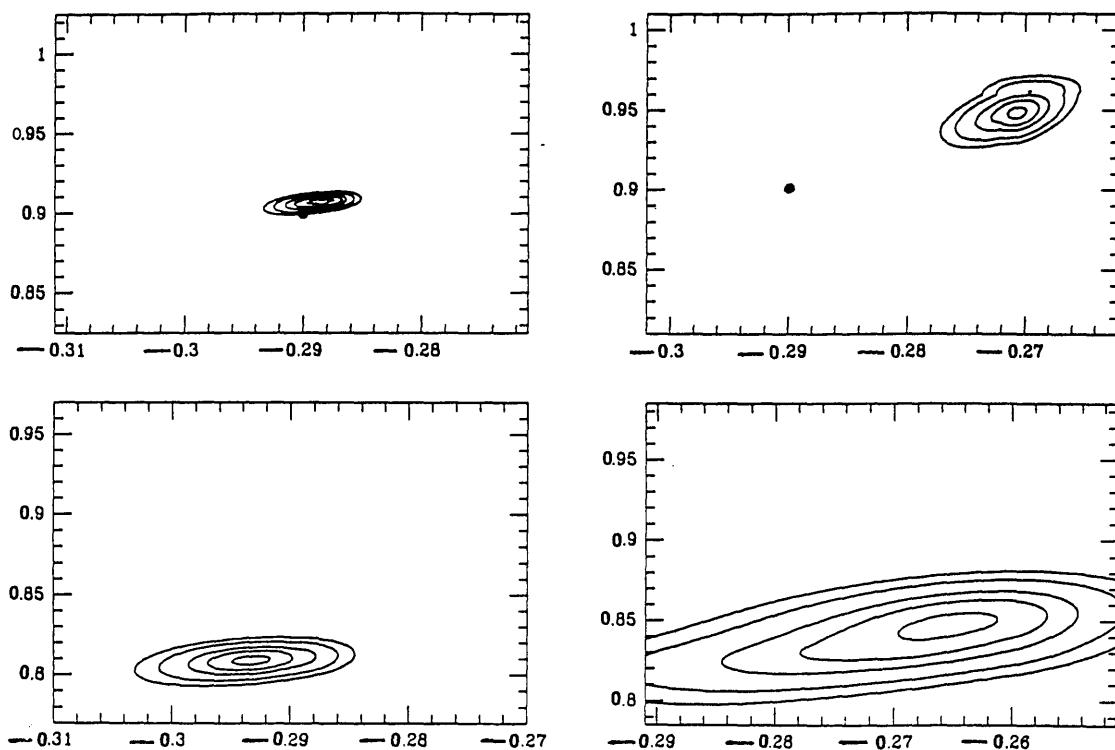


Fig. 20. Contour plots showing the difference N_1 between the observed and the computed images as a function of Z_{11} and Z_4 , with (left) and without (right) taking telescope jitter into account. The top row shows simulations with a black dot at the correct values.

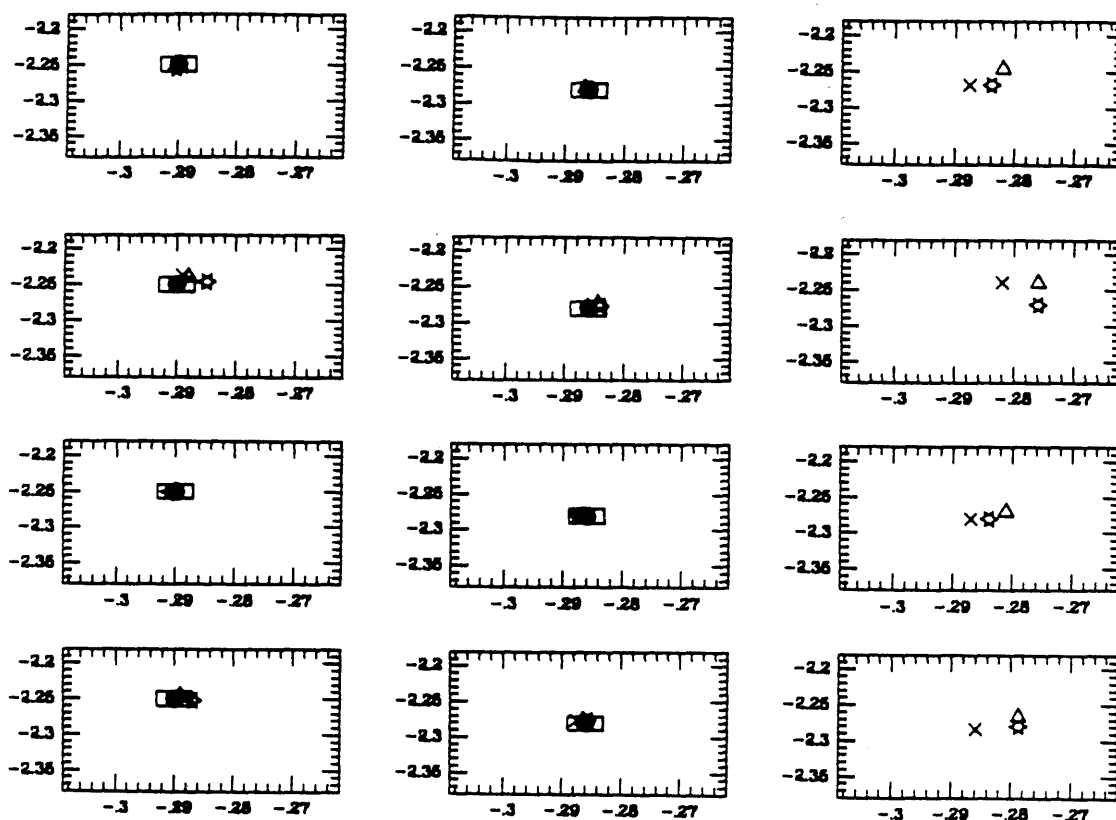


Fig. 21. Z_{11} and Z_4 estimated at focus position -260 with norms N_1 (triangles), N_2 (stars), and N_3 (crosses) for various levels of blur in the observed and computed images (see text). The black dot shows the exact Z_{11} and Z_4 values for simulations (left two columns).

is the norm mainly used throughout this work. Norm N_1 is plotted as a function of Z_{11} (horizontal axis) and Z_4 (vertical axis) expressed in micrometers rms. The contours are for 0.1%, 0.5%, 1%, 2%, and 3% excess over the minimum. Figure 20 demonstrates the effect of telescope jitter on the fitting procedure. The upper two plots show the result of a computer simulation. A defocused image was simulated with $Z_4 = 0.9 \mu\text{m}$ and $Z_{11} = -0.29 \mu\text{m}$. The image was then blurred by taking a two-dimensional running mean over 2×2 pixel squares to simulate the effect of telescope jitter. The upper right plot shows N_1 when we attempted to fit computed images to this blurred image. First, the minimum is shifted by introducing systematic errors in the parameter estimates. Second, the minimum is shallow and the contours are elongated in a direction different from the axes, producing random correlated errors. The upper left plot shows N_1 when the computed images are similarly blurred before comparison. The minimum occurs close to the correct values of the parameters. It is much deeper and the errors are uncorrelated. The lower two plots show N_1 when we attempted to fit a real image (in this case w29938). In the lower right plot no attempt was made to take telescope jitter into account. In the lower left plot computed images were blurred before comparison with the observed images. A similar effect is observed on the contour plots. Although in this case we do not know the exact values of the parameters,

the coordinates of the minimum in the left plot are clearly more reliable.

We now discuss the effect of the norm and the estimation of telescope jitter on the error of the wave-front parameter estimates.

2. Estimation of the Fitting Error

Figures 21–23 are similar to Fig. 20, but we have plotted only the value of the minimum for the different norms N_1 (triangles), N_2 (stars), and N_3 (crosses). The first two columns represent the results of simulations and the black dot indicates the correct value of the parameters. The rectangle is the estimated error box for the fitting procedure. The last column corresponds to real images and the correct value is unknown. Different figures are for different focus positions: -260 (Fig. 21), -90 (Fig. 22), and $+250$ (Fig. 23). The real images are, respectively, w29906, w33410, and w29938.

Two different types of image blur have been used, either running means or filters that match observed image blurs. Filters were obtained as follows. The observed image is Fourier transformed and the modulus of its Fourier transform is divided by the modulus of the Fourier transform of an unblurred simulation of the same image. Since the true aberrations are unknown, it is difficult to simulate an image with exactly the same aberrations. What we did is simulate several images with the same pupil geometry and with aberrations Z_4 and Z_{11} in the estimated range

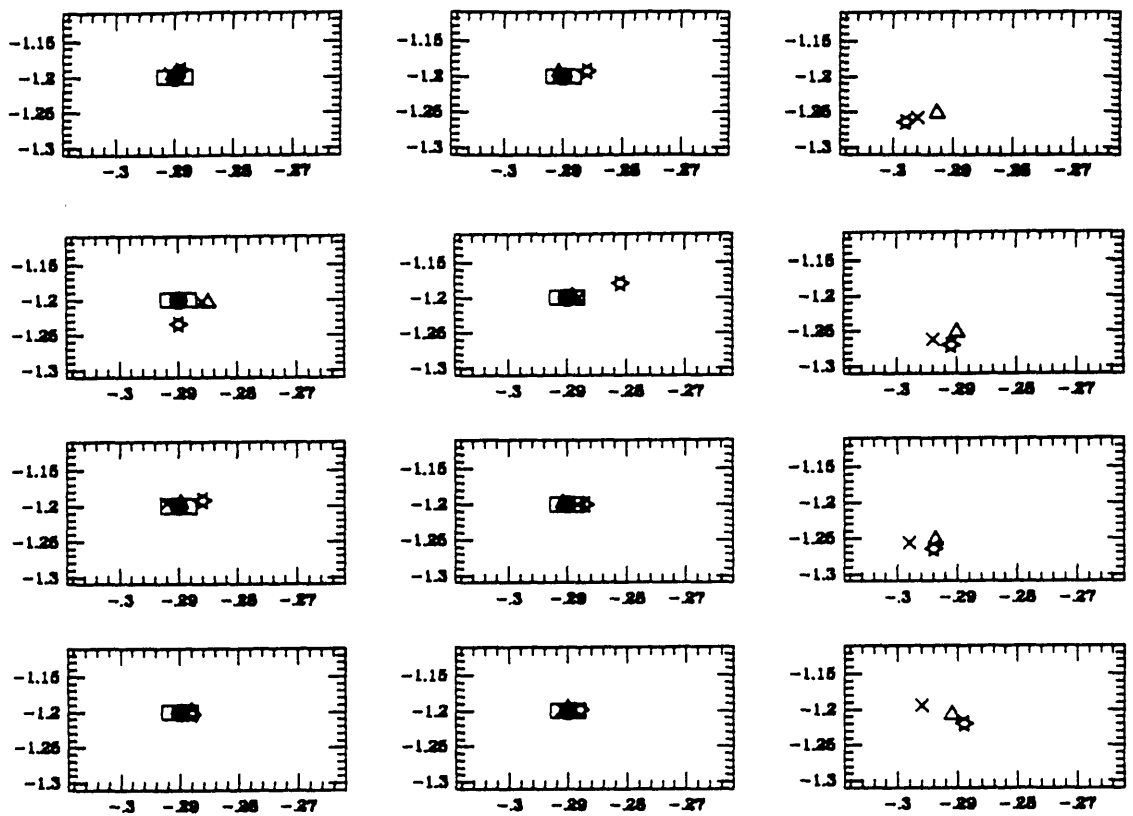


Fig. 22. Z_{11} and Z_4 estimated at focus position -90 with norms N_1 (triangles), N_2 (stars), and N_3 (crosses) for various levels of blur in the observed and computed images (see text). The black dot shows the exact Z_{11} and Z_4 values for simulations (left two columns).

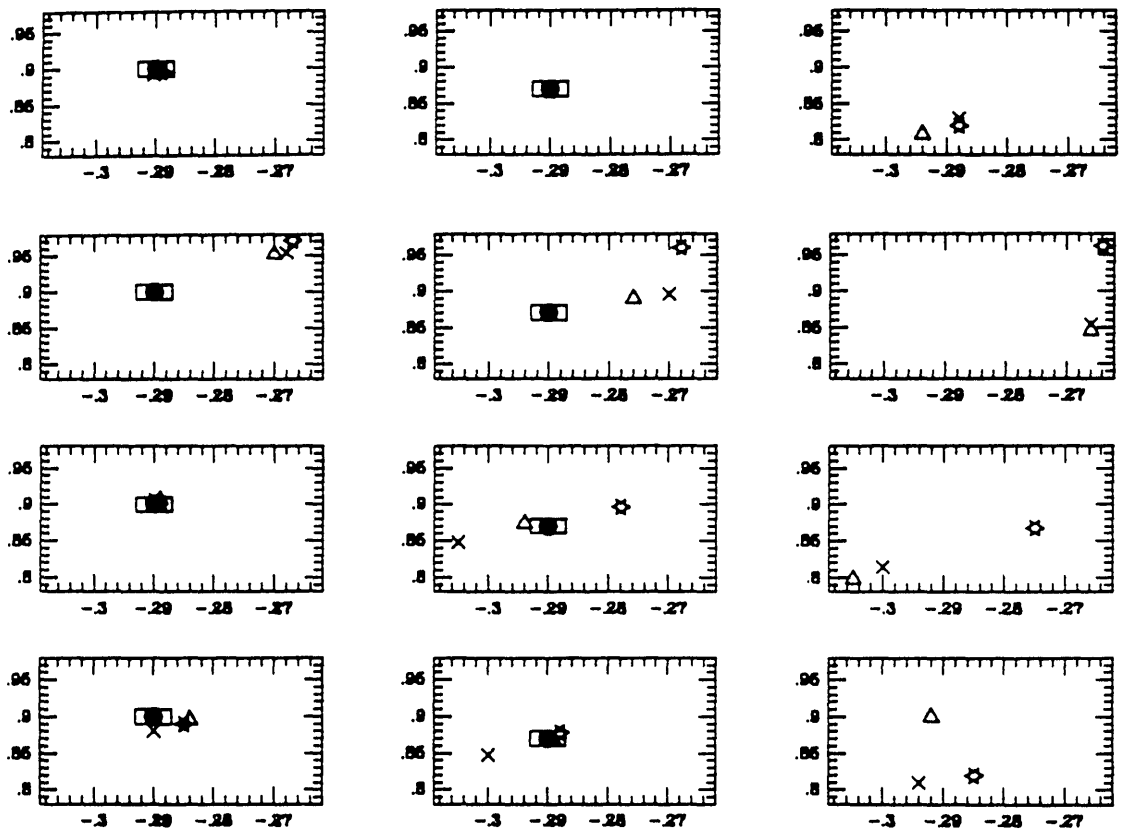


Fig. 23. Z_{11} and Z_4 estimated at focus position $+250$ with norms N_1 (triangles), N_2 (stars), and N_3 (crosses) for various levels of blur in the observed and computed images (see text). The black dot shows the exact Z_{11} and Z_4 values for simulations (left two columns).

(± 0.05 for Z_4 , 0.28 – 0.3 for Z_{11}). The result of the division was then smoothed with a running mean over 10×10 pixels. All the results looked similar. We averaged them and took the inverse Fourier transform to produce our estimated blur function. Phases were discarded because image blur essentially affects the amplitudes, and the phase is not sufficiently accurately reproduced in the simulation.

In Figs. 21–23, the top row shows the results that were obtained when image blur is properly taken into account. In the left plot unblurred simulated images were matched with unblurred estimates. In the center plot simulated images blurred with a filter were matched with estimated images blurred with the same filter. In the right plot observed images were matched with computed images blurred with the filter estimated from the same image. The next three rows are a double-input array. Different columns correspond to differently blurred input images. The left column is for simulated images with a 2×2 pixel blur. The center column is for simulated images blurred with the estimated filter. The right column is for the observed images. Different rows correspond to a different amount of blur applied to the computer-estimated images. In the first row no blur was applied; a 2×2 pixel blur was applied in the second row; a 3×3 pixel blur was applied in the third row.

3. Error Minimization

From observation of Figs. 21–23, the following conclusions can be drawn. The upper left plot is a measure of the intrinsic accuracy of the wave-front fitting procedure. The error box is an estimate of this accuracy. The three other plots in the left column describe attempts to fit images blurred by a 2×2 pixel running mean with images unblurred (first row), blurred by a 2×2 pixel (second row) or 3×3 pixel (third row) running mean. This demonstrates that

(1) Images blurred at the same level (second row) produce the smallest dispersion in the three figures. In addition, unblurred estimated images (first row) produce larger errors than overblurred estimates (third row). It is therefore essential to blur the computed images before comparison with observed images. Overblurring is preferable to underblurring.

(2) Norm N_2 (stars in the figures) is the poorest norm when we deal with unmatched blurs. This is expected because it emphasizes the importance of large differences such as those produced by different blurs.

(3) The effect of telescope jitter is less severe on the images taken inside focus (Figs. 21 and 22) compared with images taken outside focus (Fig. 23). This is also expected because images taken in focus are larger and display larger interference patterns (the distance between interfering rays is smaller on the telescope pupil). For outside-focus position $+250$ (Fig. 23), note the excessively small spherical aberration and the excessively high defocus estimate given by all the norms when telescope jitter is not taken into account (upper of the left three plots). Clearly, image blur is matched by an excess of defocus, which is in turn balanced by an underestimated spherical aberration.

The four plots in the second column in Figs. 21–23 confirm these results. The plot in the isolated upper row shows results that were obtained when the simulated image and the computer estimates are blurred by the same filter. The dispersion between the values at the three focus positions is small. In the three lower plots the dispersion becomes larger. Poor aberration estimates are obtained at focus position $+250$, especially when telescope jitter is not taken into account (upper of the central three plots in Fig. 23). Again spherical aberration is underestimated with all norms. Norm N_2 is the poorest; norms N_1 and N_3 appear equivalent.

The last column in Figs. 21–23 shows results that were obtained on real images: w29906 taken at focus position -260 (Fig. 21), w33410 taken at focus position -90 (Fig. 22), and w29938 taken at focus position $+250$ (Fig. 23). Although in this case the real value of the aberrations is unknown, similar effects can be seen. The simulation results help us to understand these results and make better decisions. They tell us we should discard results that were obtained with norm N_2 (stars). We should also discard results that were obtained without taking telescope jitter into account (upper of the three rows), which, as expected, tend to underestimate spherical aberration, especially out of focus (Fig. 23). For the inside-focus images, it is easy to give an estimate by taking into account the three other plots and the two remaining norms because the values are actually quite close. For the outside-focus image it is more difficult, and our estimate ($Z_4 = 0.83$, $Z_{11} = -0.292$) is considered unreliable (no asterisk in Table 1). For image w29906, we obtained the estimates given in Table 1 ($Z_4 = -2.27$, $Z_{11} = -0.278$) with the original Misell algorithm; these were also considered unreliable. From the plots in Fig. 21 we see that $Z_4 = -2.27$ is probably a fair estimate, but $Z_{11} = -0.278$ is clearly an underestimate in agreement with values that were obtained when telescope jitter was not taken into account (upper right plot of the 3×3 array in Fig. 21). From the right plot in the upper isolated row in Fig. 21, a more reliable estimate would be -0.285 , which is closer to our reliable values.

4. Refinements

Once defocus and spherical aberration are estimated, a similar procedure can be used to refine our wave-front tilt estimate and determine the image center as a fraction of pixel. These estimated low-order Zernike aberration terms determine the first input wave front in our Gerchberg–Saxton iteration loop. After 50 iterations small-scale wave-front aberrations appear, but, in general, the low-order Zernike terms

remain within the uncertainty in our first estimate. Only on a few occasions, when the sharpest images were processed, did we decide to change our first estimate and start new iterations until the Zernike terms in the output wave front agreed with those in the input wave front.

This work was supported by the Jet Propulsion Laboratory under contract 958893.

References

1. F. Roddier, "Curvature sensing and compensation: a new concept in adaptive optics," *Appl. Opt.* **27**, 1223-1225 (1988).
2. F. Roddier, C. Roddier, and N. Roddier, "Curvature sensing: a new wave-front sensing method," in *Statistical Optics*, G. M. Morris, ed., *Proc. Soc. Photo-Opt. Instrum. Eng.* **976**, 203-209 (1988).
3. C. Roddier, F. Roddier, A. Stockton, and A. Pickles, "Testing of telescope optics: a new approach," in *Advanced Technology Optical Telescopes IV*, L. D. Barr, ed., *Proc. Soc. Photo-Opt. Instrum. Eng.* **1236**, 756-766 (1990).
4. R. W. Gerchberg and W. O. Saxton, "A practical algorithm for the determination of phase from image and diffraction plane pictures," *Optik (Stuttgart)* **35**, 237-246 (1972).
5. J. R. Fienup and C. C. Wackerman, "Phase-retrieval stagnation problems and solutions," *J. Opt. Soc. Am. A* **3**, 1897-1907 (1986).
6. D. L. Misell, "A method for the solution of the phase problem in electron microscopy," *J. Phys. D* **6**, L6-L9 (1973).
7. D. L. Misell, "An examination of an iterative method for the solution of the phase problem in optics and electron optics. I: Test calculations," *J. Phys. D* **6**, 2200-2216 (1973).
8. D. L. Misell, "An examination of an iterative method for the solution of the phase problem in optics and electron optics. II: Sources of error," *J. Phys. D* **6**, 2217-2225 (1973).
9. R. H. Boucher, "Convergence of algorithms for phase retrieval from two intensity distributions," in *1980 International Optical Computing Conference I*, W. T. Rhodes, ed., *Proc. Soc. Photo-Opt. Instrum. Eng.* **231**, 130-141 (1980).
10. D. Morris, "Phase retrieval in the radio holography of reflector antennas and radio telescopes," *IEEE Trans. Antennas Propag.* **AP-33**, 749-755 (1985).
11. C. Roddier and F. Roddier, "Reconstruction of the Hubble Space Telescope mirror figure from out-of-focus stellar images," in *Space Astronomical Telescopes and Instruments*, P. Y. Bely and J. B. Breckinridge, eds., *Proc. Soc. Photo-Opt. Instrum. Eng.* **1494**, 78-84 (1991).
12. L. M. Kani and J. C. Dainty, "Super-resolution using the Gerchberg algorithm," *Opt. Commun.* **68**, 11-17 (1988).
13. C. Roddier and F. Roddier, "A combined approach to HST wave-front distortion analysis," in *Space Optics*, Vol. 19 of 1991 OSA Technical Digest Series (Optical Society of America, Washington, D.C., 1991), pp. 25-27.
14. C. Burrows, "Algorithms—preliminary results," in *Proceedings of the First Hubble Aberration Recovery Program Workshop, 15-16 November 1990*, R. Korechoff, ed. (Jet Propulsion Laboratory, Pasadena, Calif., 1990), paper 8.
15. V. N. Mahajan, "Zernike annular polynomials for imaging systems with annular pupils," *J. Opt. Soc. Am.* **71**, 75-85 (1981).
16. R. Lyon and P. Miller, "Phase retrieval algorithms and results," in *Proceedings of the First Hubble Aberration Recovery Program Workshop, 15-16 November 1990*, R. Korechoff, ed. (Jet Propulsion Laboratory, Pasadena, Calif., 1990), paper 13.
17. C. Roddier and F. Roddier, "New optical testing methods developed at the University of Hawaii: results on ground-based telescopes and the Hubble Space Telescope," in *Advanced Optical Manufacturing and Testing II*, V. J. Doherty, ed., *Proc. Soc. Photo-Opt. Instrum. Eng.* **1531**, 37-43 (1991).